PCCP

ROYAL SOCIETY OF CHEMISTRY

PAPER

View Article Online
View Journal

Cite this: DOI: 10.1039/d2cp01032a

An optimal acquisition scheme for Q-band EPR distance measurements using Cu^{2+}-based protein labels†

Xiaowei Bogetti,‡ Zikri Hasanbasri,‡ Hannah R. Hunter and Sunil Saxena *

Recent advances in site-directed Cu^{2+} labeling of proteins and nucleic acids have added an attractive new methodology to measure the structure-function relationship in biomolecules. Despite the promise, accessing the higher sensitivity of Q-band Double Electron Electron Resonance (DEER) has been challenging for Cu^{2+} labels designed for proteins. Q-band DEER experiments on this label typically require many measurements at different magnetic fields, since the pulses can excite only a few orientations at a given magnetic field. Herein, we analyze such orientational effects through simulations and show that three DEER measurements, at strategically selected magnetic fields, are generally sufficient to acquire an orientational-averaged DEER time trace for this spin label at Q-band. The modeling results are experimentally verified on Cu^{2+} labeled human glutathione S-transferase (hGSTA1-1). The DEER distance distribution measured at the Q-band shows good agreement with the distance distribution sampled by molecular dynamics (MD) simulations and X-band experiments. The concordance of MD sampled distances and experimentally measured distances adds growing evidence that MD simulations can accurately predict distances for the Cu^{2+} labels, which remains a key bottleneck for the commonly used nitroxide label. In all, this minimal collection scheme reduces data collection time by as much as six-fold and is generally applicable to many octahedrally coordinated Cu^{2+} systems. Furthermore, the concepts presented here may be applied to other metals and pulsed EPR experiments.

Received 2nd March 2022,
Accepted 10th May 2022

DOI: 10.1039/d2cp01032a

rsc.li/pccp

Introduction

Pulsed electron paramagnetic resonance (EPR) distance measurements[1–7] have had a major impact in a variety of biophysical contexts, including the measurement of conformational changes,[8–15] determination of relative packing in protein–protein[16–18] and protein–DNA complexes,[19,20] and the elucidation of ligand and metal binding sites in proteins.[21–23] Additionally, these experiments have been introduced both *in vitro* and in-cell.[24–27] Such measurements are enabled by site-directed spin labeling methodology that has predominantly used nitroxide spin labels.[28] Recently, several attractive schemes for labeling proteins and nucleic acids with metal ions have been developed to enhance the reach of spin labeling methodology in biophysics.[29,30] In particular, site-directed Cu^{2+} labeling of proteins can provide distance distributions that are up to five-times narrower than similar measurements using nitroxide-based labels.[31] The Cu^{2+} labeling method for protein relies on the strategic placement of two histidines which can bind to the Cu^{2+} ion. The labeling of the double-histidine (dHis) site is achieved by using either a Cu^{2+}-iminodiacetic acid[32] or a Cu^{2+}–nitrilotriacetic acid (NTA)[33] chelate to prevent non-specific binding of Cu^{2+} elsewhere in the protein. The labeling approach is facile, can be implemented in a wide variety of buffers,[34] and a range of pH.[35] In addition, distance measurements using dHis labeling and Relaxation Induced Dipolar Modulation Enhancement Spectroscopy (RIDME) can be performed at sub-micromolar concentrations.[36] The dHis–Cu^{2+} labeling method provides enhanced resolution to the multilateration of native metal binding sites,[22] measurement of relative orientations in proteins,[37] induced conformational changes,[38,39] and the measurement of site-specific dynamics even on β-sheets.[40] For DNA, a nucleotide-independent Cu^{2+} labeling approach that can directly report on backbone distances[41,42] and DNA conformational changes[43] is also available. There is also emerging work on labeling DNA with Cu^{2+} by creating a quadruplex structure.[44–46] On the other hand, due to the large spectral bandwidth of Cu^{2+}, compared to nitroxides, the sensitivity of the label is an area for improvement.

The advent of high-field instrumentation, especially at Q-band (*ca.* 35 GHz) has been particularly impactful by

Department of Chemistry, University of Pittsburgh, PA 15260, USA.
E-mail: sksaxena@pitt.edu

† Electronic supplementary information (ESI) available: Details of ESEEM measurements; ESEEM and CW-EPR spectra; simulated FS-ESE, excitation profile and DEER signal; relaxation times; primary DEER data; and distance distributions. See DOI: https://doi.org/10.1039/d2cp01032a

‡ These authors contributed equally to this work.

providing more than an order of magnitude enhancement of sensitivity compared to X-band measurements (*ca.* 9.5 GHz).[47] Overall, the improved sensitivity has been especially valuable for nitroxide based Double Electron–Electron Resonance (DEER) distance measurements. Despite this potential, distance measurements involving Cu^{2+} at Q-band have been limited, due to difficulties in the proper sampling of all orientations of the inter-spin vector in DEER.[37,44] At Q-band the spectral bandwidth of the Cu^{2+}-spectrum is *ca.* 5 GHz due to the large anisotropy of the *g*-tensor. On the other hand, the pulses that are typically used excite only a bandwidth of *ca.* 100–300 MHz[48] due to resonator and pulse amplifier limitations. Consequently, DEER measurements at a given magnetic field sample only some orientations of the inter-spin vector. To ameliorate these orientational effects, a DEER experiment at Q-band require the collection of data at different magnetic fields. For example, earlier Q-band DEER work on a dHis–Cu^{2+} labeled protein utilized seventeen different magnetic fields to obtain the same distance distribution observed using X-band DEER measurement at a single magnetic field.[37] This constraint at Q-band can often make X-band measurements more practical, despite their decreased sensitivity. On the other hand, the initial work at Q-band likely suffered from oversampling, and therefore, there is a critical need to establish the minimum number of fields and the associated averaging scheme for practical distance measurements.

In this work, we establish an optimal approach for collecting dHis–Cu^{2+}-based distance measurements at Q-band frequency by focusing on the human glutathione S-transferase (hGSTA1-1) enzyme. We first used MD simulations to identify the distance and orientational information of the Cu^{2+}-labeled sites. This information was then used as initial values to determine the number of angles excited as a function of magnetic field using a Monte-Carlo scheme. The information on angles was analyzed to establish an excitation scheme that is expected to appropriately sample molecular orientations. We then demonstrate through simulations that the minimal acquisition scheme is applicable for any possible orientation. Thus, the acquisition scheme can be used without the need for prior structural information. Finally, this scheme was validated by experiments on the protein at both Q- and X-bands, and by MD simulations.

Experimental

Protein expression, purification, and sample preparation

All experiments were performed on the S-hexylglutathione (GSHex) bound form of hGSTA1-1. The K211H/E215H mutant was expressed and purified based on the previously published protocol,[40] except the cell growth was done in Luria Broth instead of Terrific Broth media. hGSTA1-1 is a homodimer such that a single dHis mutant provides two Cu^{2+}–NTA binding sites. The purified protein was concentrated and aliquoted to *ca.* 200 μM in buffer (pH = 6.5) with 150 mM NaCl and 50 mM sodium phosphate then stored at −80 °C.

In order to prepare the EPR samples, a 10 mM Cu^{2+}–NTA stock was prepared as described previously[33,34,49] and the GSHex ligand was purchased from Sigma Aldrich. All samples in this work were prepared with 3-*N*-morpholinopropanesulfonic acid (MOPS) buffer to facilitate efficient Cu^{2+}–NTA binding to dHis.[34] Each EPR sample was prepared with 800 μM GSHex, 800 μM protein and 800 μM Cu^{2+}–NTA (a 1 : 1 : 1 ratio to ensure that the concentration of both protein and ligand are 10^4 times over K_D of GSHex to hGSTA1-1)[50] in 50 mM MOPS buffer in D_2O (pH = 7.4) with 100 mM NaCl. All samples were incubated at 4 °C for 35 min to achieve maximum loading efficiency, and subsequently flash frozen in liquid MAP-Pro Propylene/propane gas with 50% D_6-glycerol added as cryoprotectant. A step-by-step protocol for spin labelling and freezing has been published recently.[49]

MD simulation of dHis–Cu^{2+}–NTA labeled protein

The MD simulation was performed starting from the crystal structure of GSHex-bound hGSTA1-1 (PDB:1K3L).[51] To generate parameters for the ligand GSHex, the PDB of GSHex was extracted from the crystal structure of liganded hGSTA1-1. Using the Antechamber package in Amber18, charges were derived using the AM1-BCC method.[52,53] Force field angles and dihedral terms were assigned with the General Amber Force Field (GAFF).[54] Sites 211 and 215 of each monomer were mutated to histidine for the incorporation of Cu^{2+}–NTA. The force fields for Cu^{2+}–NTA have been developed in previous work.[55] The hGSTA1-1 was simulated with the ff14SB AMBER force field.[56] Solvent waters were treated with the TIP3P water model.[57] The labeled protein was solvated in a cubic box with the box size of *ca.* 60 Å^3. Sodium and chloride ions were added to neutralize the system. The MD simulation was performed with the pmemd program as part of the AMBER18 software package. The solvated system was first energy minimized with a harmonic force constant applied to the protein and ligand, which was gradually released from 20 to 0 kcal mol^{-1} Å^{-2} over 12 000 steps. The energy minimized system was then equilibrated using a Berendsen barostat at 298 K for 3.2 ns with a decreasing harmonic force constant from 20 to 0 kcal mol^{-1} Å^{-2}.[58] The system was then gradually heated from 0 to 298 K. Equilibration was reached after 2 ns. The simulation at the production phase was maintained at 298 K by Langevin thermostat using a 5.0 ps^{-1} collision frequency and collected for 200 ns. A 2 ps time step for motion integration was used for equilibration and production simulations. The system pressure was kept at 1 atm with a pressure relaxation time of 1.0 ps. The SHAKE algorithm was used to restrain the bonding to hydrogens. Periodic boundary condition and particle mesh Ewald were applied to accurately treat the long-range electrostatic interactions.

Monte-Carlo simulation

To build an *in silico* model of our sample, we implemented a home-written Python[59] code, available at the Saxena Lab GitHub (github.com/SaxenaLab/MonteCarloSimulationCopper/). The process starts with the generation of 10 000 vectors, representing $g_\parallel$ of Cu^{2+} spins (Spin A). For each Spin A, we generated another spin (Spin B) separated by a vector of length *r*. The $g_\parallel$ tensor of Spin B is rotated by an angle γ with respect to the $g_\parallel$ tensor of

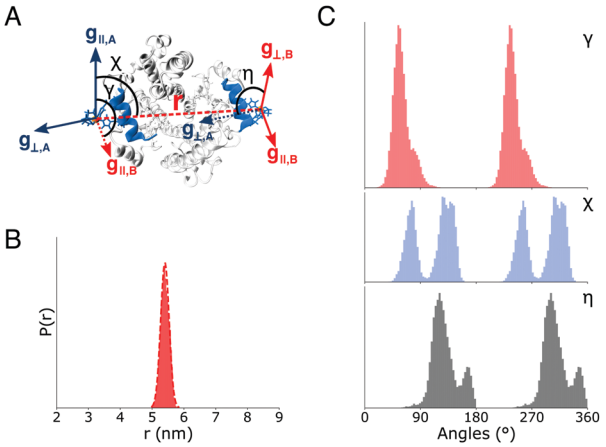

Fig. 1 (A) Definition of g-tensors and relative angles within dHis–Cu^{2+}–NTA labeled hGSTA1-1. γ is the angle between $g_{\parallel,A}$ and $g_{\parallel,B}$; χ is the angle between $g_{\parallel,A}$ and the interspin vector r; and η is the angle between $g_{\perp,A}$ and $g_{\perp,B}$. (B) Cu^{2+}–Cu^{2+} distance distribution from a 200 ns MD run. The most probable distance is 5.3 nm, and the standard deviation is *ca.* 0.2 nm. The distance distribution was reasonably reproduced by a Gaussian shown by the red dashed line. (C) The distribution of each orientational angle.

Spin A. Similarly, the $g_\perp$ of Spin B is rotated by an angle η with respect to the $g_\perp$ of Spin A. For each pair, another vector, representing the inter-spin vector, is generated with an orientation of χ with respect to the $g_\parallel$ tensor of Spin A. The angles γ, χ, and η, defined pictorially in Fig. 1, were sampled from three different Gaussian distributions defined by the user. These vectors represent 10 000 spin-pairs of Cu^{2+}-labeled hGSTA-1 sample. After generating the vectors, the spin-pairs were then randomly rotated to simulate spin-pairs with random orientations.

From each spin, we calculated the effective g and hyperfine interaction term, A, as a function of angle, ϕ, between the applied magnetic field and $g_\parallel$ with the following equations:[60]

$$g(\phi) = \sqrt{g_\perp{}^2 \sin^2\phi + g_\parallel{}^2 \cos^2\phi} \quad (1)$$

$$A(\phi) = \frac{\sqrt{A_\perp{}^2 g_\perp{}^4 \sin^2\phi + A_\parallel{}^2 g_\parallel{}^4 \cos^2\phi}}{g_\perp{}^2 \sin^2\phi + g_\parallel{}^2 \cos^2\phi} \quad (2)$$

Both the g and A tensors were experimentally determined, as shown in Fig. S1 (ESI†). The effective g and A values of each spin were then used to calculate the resonant field, B_{res,m_I}, of the spin using the following equation:

$$B_{\mathrm{res},m_I} = \frac{h\nu - Am_I}{g\beta_e} \quad (3)$$

where h is Planck's constant, ν is the microwave frequency, β_e is Bohr Magneton, and m_I is the nuclear quantum number. For our analysis, we set ν as 34.15 GHz to approximate a Q-band frequency. Then, at each resonant field, we built a Lorentzian line-shape with an arbitrary maximum intensity of 1 and a broadening parameter, β, of 40 G. The Lorentzian curve is built as follows:

$$I(B) = \sum_{m_I} \frac{\beta^2}{\left(B - B_{\mathrm{res},m_I}\right)^2 + \beta^2} \quad (4)$$

where β is the broadening parameter. By summing all the Lorentzian functions from all spins, we were able to generate a field-swept spectrum. The parameter β was chosen as 40 G to best fit with experimental field sweep (*cf.* Fig. S2, ESI†).

In addition to the field-swept spectra, we used $I(B)$ to determine whether a spin with a given ϕ can be excited at a given field. Specifically, we consider a spin to be excited only when the intensity of $I(B)$ at a specific field is above a defined threshold parameter, α. The α was set to 0.4 in our analysis to ensure optimal sampling of the number of spins (*cf.* Fig. S3, ESI†). The sampling of number of spins is also dependent on the choice of β. As $I(B)$ becomes broader due to an increase in β, α must be adjusted to maintain optimal sampling of the spins. Therefore, both α and β are critical in our simulations. More details for the choices of α and β are provided in the results section and the ESI.†

Excitation profile of θ

To understand the origin of orientational selectivity, the excitation of θ angles can be studied. θ is defined as the angle between the inter-spin vector, r, and the applied magnetic field B_0 (Fig. 2A). To include orientational effects in DEER experiments, DEER signal for a two-Cu^{2+} system can be expressed as:[61]

$$V(t)_{\mathrm{intra}} = 1 - \int\int^{\lambda} \left(1 - \cos\left[\frac{k}{r^3}(1 - 3\cos^2\theta)\right]\right) P(r)\xi(\theta)\mathrm{d}\theta\mathrm{d}r \quad (5)$$

where λ is the modulation depth, k is the constant containing the g values of the two spins, r is the distance between the two spins, $P(r)$ is the distribution function of the distance, and $\xi(\theta)$ is the

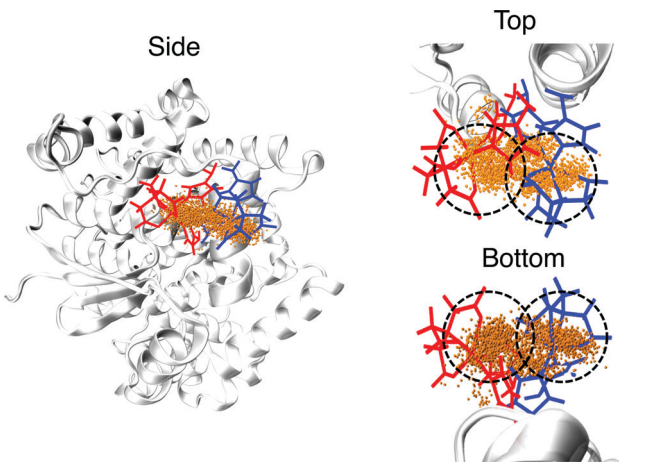

Fig. 2 Cu^{2+} spatial distribution. The helix α9 shows two conformations (indicated by Cu^{2+}–NTA conformations in red and blue sticks) in MD that result from a slight turn of the helix around the loop. Thus, the Cu^{2+} atom (yellow dots) shows a bimodal spatial distribution, indicated by the two black dashed circle, leading to a bimodal distribution in χ below 180°.

geometrical factor describing the probability of exciting θ, which is defined as:[62]

$$\xi(\theta)=\frac{1}{2}\sum_{m_{I_1},m_{I_2}}\langle k_{xa}{}^3k_{xb}{}^2\sin\varphi_{1a}(1-\cos\varphi_{2a})(1-\cos\varphi_{3b}) + k_{xb}{}^3k_{xa}{}^2\sin\varphi_{1b}(1-\cos\varphi_{2b})(1-\cos\varphi_{3a})\rangle_{\phi,\delta\omega_1,\delta\omega_2} \quad (6)$$

where m_{I_i} is the nuclear quantum number of the ith spin, k_{xa} and k_{xb} are defined as the ratio of the resonance frequency of the excited spins *versus* the frequency at observer and pump frequency, respectively, φ_{ia} is the flip angle of the first spin by the ith pulse, φ_{ib} is the flip angle of the second spin by the ith pulse, and $\delta\omega_i$ is the inhomogeneous broadening of the observer or the pump pulses. If all orientations of the spin-labeled molecules are properly sampled, the geometrical factor $\xi(\theta)=\sin(\theta)$.

EPR measurements

To determine g and A-tensors and the coordination environment for Cu^{2+}–NTA labeled liganded hGSTA1-1, continuous wave (CW) EPR experiment and three-pulse electron-spin echo envelope modulation (ESEEM) experiments[63,64] were performed with a Bruker ElexSys E680 X-band FT/CW spectrometer with a Bruker EN4118X-MD4 resonator. The CW-EPR experiment was performed at 80 K and the ESEEM experiment was performed at 20 K. The CW was collected at microwave frequency *ca.* 9.70 GHz, with a modulation frequency of 100 kHz, modulation amplitude of 4 G, and a sweep width of 2000 G centered at 3100 G. A total of 1024 data points were collected with an attenuation of 30 dB, conversion time of 20.48 ms, and data was averaged over 50 scans. The X-band sample contains 100 μL of 400 μM hGSTA1-1 dimer, 800 μM GSHex and 800 μM Cu^{2+}–NTA in 50 mM MOPS buffer prepared with D_2O (pH = 7.4) with 100 mM NaCl, 50% D_6-glycerol, placed in quartz tube with I.D. = 3 mm and O.D. = 4 mm. The CW spectrum was simulated with EasySpin.[65] More details of the ESEEM measurements are provides in ESI.†

To acquire distance distributions between labels within liganded hGSTA1-1, four-pulse DEER experiments were performed at 18 K at both X-band and Q-band frequencies.[1] For the X-band DEER, the measurement was performed on a Bruker ElexSys E680 X-band FT/CW spectrometer equipped with a Bruker EN4118X-MD4 resonator and a 1 kW amplifier. For the Q-band DEER, the measurements were performed with a Bruker ElexSys E580 X-band FT/CW spectrometer with a Bruker ER5106-QT2 resonator and a 300 W amplifier. The pulse sequence used was $(\pi/2)\nu_A-\tau-(\pi)\nu_A-\tau+t-(\pi)\nu_B-T-t-(\pi)\nu_A-T-$echo.[66] For X-band DEER, rectangular pulses were used. The lengths of the observer $(\pi/2)\nu_A$ and $(\pi)\nu_A$ were 8 and 16 ns, respectively. The pump pulse had a length of 16 ns. The interval, t, was incremented by a step size of 30 ns over 202 points. For Q-band DEER, the $(\pi/2)\nu_A$ and $(\pi)\nu_A$ pulses were rectangular pulses with lengths of 12 ns and 24 ns, respectively. To increase the modulation depth, an 80 ns chirp pulse was used for the pump pulse. The pump pulse was set with a frequency from −200 MHz to −100 MHz relative to the observer frequency. A 16-step phase cycling was used. The duration, t, was incremented with the same step size as X-band DEER over a total of 237 points. We performed DEER measurements with pump pulses placed 116 G, 566 G, and 746 G, lower than the magnetic field with the highest intensity of the Field Swept Electron Spin Echo (FS-ESE) Spectrum. To further test the sufficiency of the collection scheme, seven additional DEER were collected with pump pulse placed at fields that are *ca.* 641 G, 516 G, 466 G, 416 G, 334 G, 250 G, and 165 G lower than the magnetic fields with the highest intensity of the FS-ESE spectrum. DEERAnalysis2021[67] was used to analyze the data.

Results and discussion

In this work, we focused on the conformation of the α 9 helix of hGSTA1-1 in the presence of ligand GSHex. The conformation and dynamics of this helix is intimately related to the function of this protein.[68,69] For this purpose, we generated a K211H/E215H hGSTA1-1 mutant, as described in previous work,[38] which was subsequently labelled with Cu^{2+}-NTA. Due to the homodimeric nature of hGSTA1-1, a single dHis mutant provides two labelled sites, one on each subunit, for distance measurements.

MD simulation provides initial angle and distance distributions

We first established the anticipated distance distribution and orientational distribution of the *g*-tensors of the two Cu^{2+} sites using MD simulations. The orientation distribution is characterized by the three angles γ, χ, and η, shown in Fig. 1A. The angle, γ, is defined as the angle between $g_{\parallel,A}$ and $g_{\parallel,B}$; χ is the angle between $g_{\parallel,A}$ and inter-spin vector r; and η is the angle between $g_{\perp,A}$ and $g_{\perp,B}$. For Cu^{2+} distances, orientational selectively is strong for narrower orientational distributions.[37,55,61,70] Therefore, a reference model providing Cu^{2+}-Cu^{2+} distances with relative orientations is pertinent to our analysis. We performed a 200 ns MD simulation of GSHex-bound hGSTA1-1 (PDB: 1K3L)[51] with Cu^{2+}–NTA labels introduced into α9 at site K211H/E215H. In the MD simulation, we used the force fields parameters for dHis–Cu^{2+}–NTA that were recently developed.[55]

From the MD simulation, we obtained the distance, r, between the two Cu^{2+} centers, plotted in Fig. 1B. The Cu^{2+}–Cu^{2+} distance distribution is centered around 5.3 nm, with a standard deviation σ_r of *ca.* 0.2 nm. We then extracted the relative orientations of the Cu^{2+} spin labels from the MD trajectory. The imidazole nitrogen atoms bind to Cu^{2+} equatorially, leading to the $g_\parallel$ perpendicular to the equatorial plane. The directions of $g_\parallel$ and $g_\perp$ in the dHis–Cu^{2+}–NTA complex are defined in ESI† (Fig. S4). The distributions of γ, χ, and η are shown in Fig. 1C. For γ, χ, and η the distribution under 180°, there is an identical distribution at γ + 180°, χ + 180° and η + 180°, respectively. This n° and n° + 180° distribution pattern is expected given that $g_\parallel$ can be oriented "up" or "down" with respect to the equatorial plane due to the symmetry of the d_{z^2} orbital that the electron spin resides in. On the other hand,

χ shows a bimodal distribution below 180°. A more careful examination of the MD traces, shown in Fig. 2, suggests that the Cu^{2+} adopts two preferred orientations, likely due to conformations of the α9 helix, as has observed previously.[38,40]

Finally, the standard deviation of γ, χ, and η are 14°, 10° and 21°, respectively. This standard deviation for these angles is consistent with earlier estimates on Cu^{2+} coordination to dHis sites in proteins and polynucleic acids that were obtained using a combination of MD and density functional calculations.[29,55,71] In these systems, the Cu^{2+} coordination is elastic leading to a fluctuation in the bond angles and bond lengths of the Cu^{2+} coordinating atoms. Such fluctuations create a distribution in the directions of $g_{\|}$ which generates a distribution in the γ, χ, and η angles.

The MD simulation, thus provide reasonable estimates for the standard deviations for the three angles, γ, χ, and η. The greater the value of these standard deviations the lower the effects of orientational selectivity.[61,70]

The optimal DEER collection scheme

Next, we used the information on expected orientation widths for dHis–Cu^{2+} labelled proteins obtained from MD simulations to devise an optimal collection scheme. First, we used Monte-Carlo methods[72] to generate an *in silico* sample containing 10 000 Cu^{2+}-labeled proteins, as shown in Fig. 3. Details are in the Experimental section. Each blue and green dot in Fig. 3A represents Spin A and Spin B, respectively, in a doubly Cu^{2+} labeled protein. The *g*-tensors and the orientation of the inter-spin vector, r, are shown in Fig. 3B. In the *in silico* sample, each set of Spin A, Spin B, and r is arranged with a given set of γ, χ, and η and r sampled from Gaussian distributions shown in Fig. 3D. For γ, χ, and η, we used the most probable angles of 75°, 60° and 129°, respectively, as the mean angles for their respective Gaussian distributions. Note, that we ignored the bimodality for χ and the inherent symmetry for each angle (*cf.* Fig. 1). We also used a standard deviation of 10° for each angle, which is a conservative estimate for the dHis–Cu^{2+} labeled proteins.[29,37,55] Together, these choices make the *in silico* sample more prone to orientational selectively. Fig. 3C shows a count of the number of inter-spin vectors as a function of the angle, θ, between the inter-spin vector and the applied magnetic field. This probability distribution is sinusoidal, as expected for a random distribution.

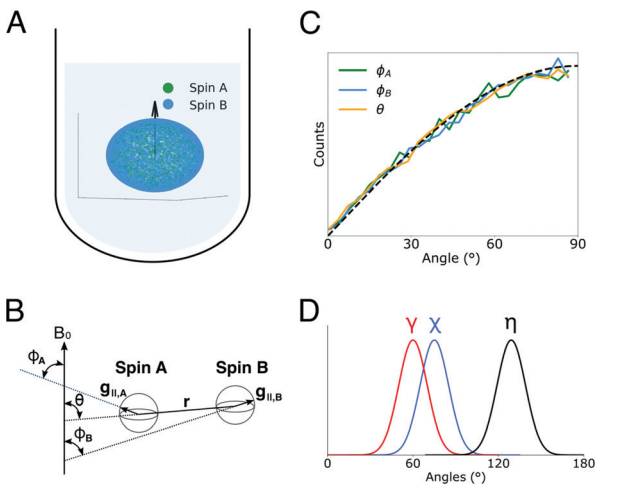

Fig. 3 *In silico* sample consisting of randomly oriented vectors with two spins. (A) When all doubly labeled molecules are randomly oriented, the orientation of inter-spin vector, r, will also be random, as depicted by the spherical figure. The black arrow represents the applied magnetic field, while blue and green dots on the sphere represent orientations of the $g_{\|}$ of Spin A and Spin B generated by the Monte-Carlo simulation. (B) A vector representation of two spins separated by inter-spin vector, r. The orientations of each spin can be described with ϕ while the orientation of r can be described with θ. (C) Plot of the distribution of θ, ϕ_A and ϕ_B in the Monte-Carlo simulation. The plot follows a sinusoidal curve depicted by the black dashed line, consistent with a random distribution. (D) Gaussian distributions of γ, χ and η used for the Monte-Carlo simulations.

To obtain a robust Q-band DEER, the data must be acquired in a manner that samples the θ distribution shown in Fig. 3C.[62] On the other hand, the pulses in DEER are finite and can excite only some θ values at a given magnetic field. The excited θ values are dependent on the Cu^{2+} orientations, ϕ_A and ϕ_B, that are excited by the pump and observer pulses in DEER. Therefore, we first identified fields that can efficiently excite the largest number of ϕ angles.

We used the *in silico* sample to calculate the resonant fields, B_{res,m_I}, of each Cu^{2+}-spin (A or B) as a function of ϕ_A or ϕ_B using eqn (1)–(3). From this information a DEER signal can also be easily calculated. At each resonant field, we built a Lorentzian line-shape as a function of the magnetic field, $I(B)$, described by eqn (4). Then, we summed each Lorentzian to build a field-swept spectrum, shown in Fig. 4A. Since each Lorentzian can be identified with the angle, ϕ, the number of ϕ excited at a given field can be calculated as:

$$\Phi(B) = \int_{0^\circ}^{90^\circ} \left(\begin{cases} 1, & I_\phi(B) \geq \alpha \\ 0, & I_\phi(B) < \alpha \end{cases} \right) \sin\phi \mathrm{d}\phi \qquad (7)$$

where α is an intensity-threshold parameter. The expression of $\Phi(B)$ contains two terms. The bracketed first term represents a counter recognizing whether a ϕ value can be excited at a given field. The ϕ value is excited only when $I_\phi(B)$ is greater than or equal to α. The second term describes the relative probability of spins for a given ϕ. Overall, $\Phi(B)$ quantifies the number of ϕ excitable at a given magnetic field. The curve of $\Phi(B)$ is shown in Fig. 4A. We will refer to this curve as the Φ curve for the rest of this document. The Φ curve depends on the choice of α and breadth of the Lorentzian, β. The breadth of each Lorentzian was chosen by fitting the experimental FS-ESE spectrum of hGSTA1-1 (*cf.* Fig. S2, ESI†). The optimal value of α, was determined by examining the number of excited spins as a function of α for several different fields across the simulated FS-ESE spectrum (*cf.* Fig. S3, ESI†). For a β of 40 G, an α of 0.4 leads to a stable count of spins at different fields. The optimal value of α for several values of β are shown in Fig. S3 (ESI†).

Fig. 4A shows the Φ curve generated for the *in silico* sample shown in Fig. 3A. The value of $\Phi(B)$ (dotted lines) is overlaid on the simulated FS-ESE spectrum. The maximum number ϕ

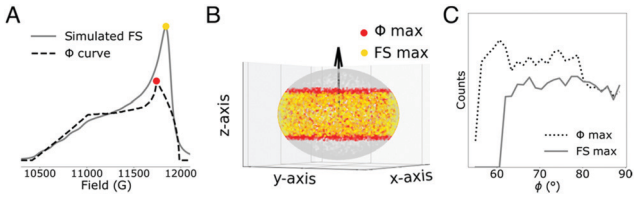

Fig. 4 (A) The spectrum in solid grey shows the simulated field-swept spectrum while the dotted line is the Φ curve described by eqn (7). The Φ curve represents the number of ϕ excited at a given field. The max of both the field sweep and the Φ curve is marked by a yellow circle and a red circle, respectively. (B) Each dot on the sphere represents ϕ of a spin in the Monte-Carlo simulation. The yellow dots represent the spin-pairs excited when DEER is performed at the maximum of the field sweep. In contrast, the red dots represent the spin-pairs excited when DEER is performed at the maximum of the curve. (C) Number of excited spins in DEER *versus* angle at the two magnetic fields.

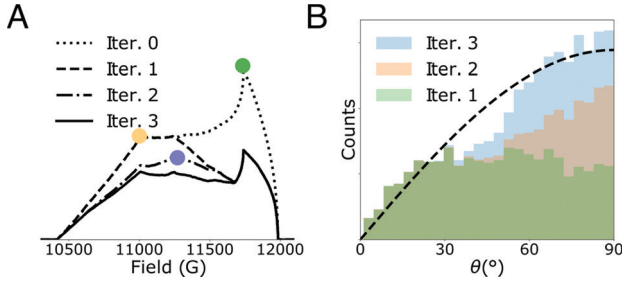

Fig. 5 (A) The curve showing the number of excitable ϕ angles *versus* magnetic field. After excitation at one field, the spin-pairs that were excited were removed to generate the curve for subsequent iterations. The maximum ϕ angle for each iteration is labeled with a dot. We iterated this process until residual ϕ angles cannot be further reduced, and this curve is shown by the black solid line. (B) Excitation profile of θ angles. The black dashed sinusoidal curve depicts the ideal excitation of θ, and the histogram shows the cumulative θ excitation after each DEER at the three identified fields.

angles are excited at a field of 11 738 G (shown by red circle on Fig. 4A), about 100 G lower than the maximum of the FS-ESE spectrum. To exemplify this point, we determined the spin-pairs excited by DEER at either the max of the Φ curve, defined as $B_{\phi 0}$, or the max of the FS-ESE spectrum. For simplicity, we assumed a square excitation profile from hyperbolic secant CHIRP pulses.[73] Specifically, we first identified the spins that can be excited by a pump pulse with a bandwidth of 100 MHz, which is set either at the maximum of the Φ curve or at the maximum of the field sweep. Next, we identified the spins that can be excited by a *ca.* 38 MHz observer pulse at the field 54 G lower than the pump field. These pulses are chosen to replicate a reasonable DEER on a commercial resonator that has *ca.* 200 MHz bandwidth. Finally, we identified the spins from the pump excitation that are paired with the spins from the observer excitation. These spin-pairs in our *in silico* sample contribute to the intra-molecular DEER signal at a given field.

The ϕ angles excited at $B_{\phi 0}$ (red dot) *versus* the maximum of FS-ESE spectrum (yellow dot) are shown in Fig. 4B. At the maximum field sweep intensity, the excited spin-pairs have ϕ range of *ca.* 62° to 90°. In contrast, a more extensive range of ϕ from *ca.* 56° to 90° can be excited at the maximum of the Φ curve. The increase in the number of ϕ is due to the large parallel component of the hyperfine tensor, $A_{\parallel}$. More importantly, this observation indicates that DEER at 100 G lower than the maximum of ESE-FS spectrum is the most optimal for probing the largest number of ϕ for Cu^{2+}-labeled systems.

Fig. 5B shows the distribution of θ that is sampled at $B_{\phi 0}$ (green histogram) by DEER. Data at only this field is clearly insufficient to achieve ideal excitation, which is shown by the dashed line. Therefore, we identified additional fields that can excite the rest of the spin-pairs. Fig. 5A, shows the recalculated Φ curve, labeled as Iteration 1, that excludes spins that are excited by the DEER at $B_{\phi 0}$. The maximum of the resultant Φ curve, $B_{\phi 1}$, is shown by the orange dot on the curve. The field, $B_{\phi 1}$, which is *ca.* 827 G lower than the maximum of the FS-ESE spectrum, represents a field that can excite the largest number of ϕ angles from the unexcited spins. We repeated the identification of the θ angles that are sampled at the additional field by DEER, shown as the orange histogram in Fig. 5B. Measurement of DEER at the additional fields improve θ sampling, especially for angles between 60° to 90°. We reiterated this process and identified a new maximum at a field, $B_{\phi 2}$, which is *ca.* 580 G lower than the maximum of the FS-ESE spectrum. From these three fields, we see that the overall distribution of sampled θ is reasonably close to ideal, indicating that the three identified fields are the most promising for Cu^{2+} DEER.

The three identified fields are based on the Φ curve. Note, however, that a change in the linewidth parameter, β, can potentially affect the Φ curve [*cf.* eqn (4)]. To test the robustness of our approach, we calculated the Φ curve for different values of β. Details are provided in ESI.† For each β, we determined the value of α that ensures optimal sampling of excited spins as shown in ESI† (*cf.* Fig. S3). As shown in Fig. S3 (ESI†), the shape of Φ curve and the resulting three identified fields remain consistent with different β. These results provide further credence to the Φ curve method. However, it is evident from Fig. 5A that there are still residual ϕ angles that are not excited even after four iterations.

To gain further insight, we visualized the orientations of unexcited spin-pairs, Spin A and Spin B, throughout the sample in each iteration, shown in Fig. 6. Initially both Spin A and Spin B have diverse orientations. After the first iteration, there are no spin-pairs that have both spins at ϕ of *ca.* 56° to 90°. After the second iteration, there are no spin-pairs where both spins are in the region of ϕ between 0° to *ca.* 42°. Finally, after the third iteration, the leftover spin-pairs only consist of A spins with ϕ between *ca.* 56° to 90° that are paired with B spins with ϕ between 0° and *ca.* 56°. In other words, the final unexcited spin-pairs primarily consisted of A spins oriented to the perpendicular region while paired with B spins oriented to the parallel region. Consequently, the resonant fields of most unexcited spin-pairs are too far apart to be excited by conventional DEER with a resonator bandwidth of 200 to 300 MHz.

Quantitatively, we found that DEER at the three fields cannot excite *ca.* 4500 spin-pairs out of 10 000 spin-pairs. However, we observed *ca.* 800 leftover spin-pairs that have ϕ around 56° for both Spin A and Spin B. These 800 spin-pairs

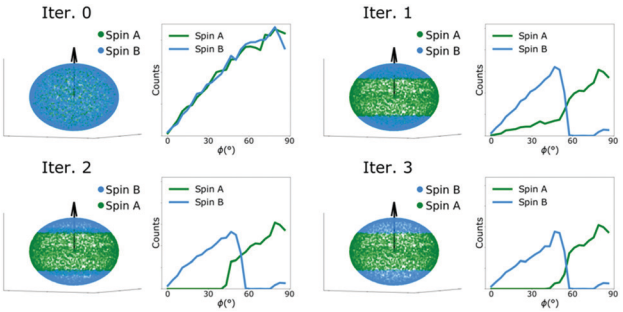

Fig. 6 Each spherical figure shows the ϕ angles of unexcited Spin A and Spin B at each iteration. The number of unexcited spins *versus* angle ϕ for Spin A and B is also shown. Initially, the orientations of unexcited Spin A and Spin B follows the same distributions as Fig. 3C. However, the first DEER at $B_{\phi 0}$ excited spin pairs that have both Spin A and B in the region of ϕ between *ca.* 56° and 90°. As a result, the leftover spins in that ϕ region only consist of Spin A (*cf.* Iter. 1) that are paired to Spin B outside of that ϕ region. In Iteration 2, the unexcited spins in the region of ϕ between 0° and 46° only consist of Spin B which are paired to Spin A in a region of ϕ above 46°. After three DEERs in Iteration 3, Spin A and Spin B are largely isolated into two different regions of ϕ.

can be excited by a fourth DEER at a field between $B_{\phi 1}$ and $B_{\phi 3}$ (*ca.* 338 G lower than the maximum of the FS-ESE spectrum). In this case, the fourth DEER only improves the sampling of θ slightly (*cf.* Fig. S5, ESI†).

Next, we simulated the Q-band DEER signal by summing up the contribution from each spin pair that was excited at the three fields. The simulated DEER is shown by the solid blue line in Fig. 7. Superposed on the curve is the ideal DEER signal (black dashed line) if all possible spin pairs were excited. Comparison of the two traces indicates that DEER experiments performed at the three identified fields are sufficient to obtain the appropriate modulations in the time-domain signal. Furthermore, an additional DEER does not significantly improve the DEER signal (*cf.* Fig. S5, ESI†).

Note, the case shown in Fig. 7 has been calculated for the orientational distribution shown in Fig. 3D. In order to ensure that the results are general, we calculated DEER traces for 125

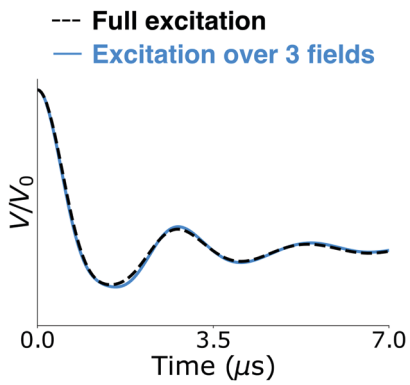

Fig. 7 Simulated averaged DEER time trace using the optimal collection method in solid blue line is compared to an ideal DEER time trace with all spins excited (black dashed line). The simulation assumes a Gaussian distance distribution with mean distance = 5.3 nm and σ_r = 0.2 nm.

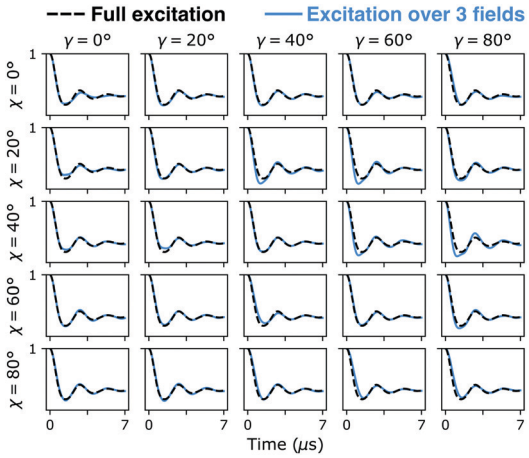

Fig. 8 Averaged DEER time traces (blue) simulated for the optimal DEER collection method compared to full excitation (black dashed). The simulation set η = 0° and $\sigma_\gamma = \sigma_\chi = \sigma_\eta$ = 10, and iterates through γ and χ from 0° to 90°.

combinations of angle χ, γ and η. In each case, the standard deviation of each angle was 10°. Fig. 8 shows simulated DEER signal with $\eta = 0° \pm 10°$, and for several different values of χ and γ that range from 0° to 90°. Simulations for $\eta > 0°$ are shown in ESI† (*cf.* Fig. S6–S9). For all orientations the summed DEER signal averaged over the three identified fields is reasonably identical to the ideal DEER time trace. However, we noticed deviations between the simulated DEER time trace and the expected time trace in a small number of cases (4 out of 125 cases) when $\eta = 0°$, $\chi = 20°$, $\gamma = 40°$ and 60°; $\eta = 0°$, $\chi = 40°$, $\gamma = 60°$ and 80°. To evaluate the significance of the discrepancy in distance distributions, we analyzed the DEER time traces with DeerAnalysis21.[67] In the distance analysis, random noise was added to the DEER signals to represent real-life measurements. We show, in Fig. S10 (ESI†), that the resulting most probable distance as well as the distribution shape generally agree with the expected distance distribution. However, in these cases, a small peak at with an intensity roughly 10% of the main peaks is observed, due to residual orientational effects. This feature originates from the 800 spin-pairs that remain unexcited. In these cases that contain a small feature, an additional DEER with pump pulse place 338 G lower than the maximum of FS-ESE spectrum is sufficient to suppress the minor peak (*cf.* Fig. S10, ESI†). Overall, DEER measurements at three magnetic fields are valid in most cases, but an additional DEER measurement may be useful to allow confident interpretation of any minor peaks in the distance distribution. The scheme is not dependent on distances of the system [eqn (6)]. Therefore, no prior knowledge of distances or structures are required.

Assumptions and generality of the acquisition scheme

The modeling is encouraging and suggests that three magnetic fields might be sufficient to acquire robust DEER data for Cu^{2+} under the following conditions. First, the parallel component of the hyperfine tensor should be *ca.* 161 G. Such large values of hyperfine, which are typical for many octahedrally coordinated

Cu^{2+} centers,[74–76] ensure that many orientations are excited at a given magnetic field. Second, the standard deviation of the orientational distribution is *ca.* 10° or larger. The value of the standard deviation is consistent with expectations for sites with moderate binding affinity such as dHis.[37,55,77,78] However, for substantially larger orientational distributions, as seen for the Cu^{2+}-2,2′-dipicolylamine DNA label,[29,79] a DEER at a single field is sufficient. On the other hand, more fields may be needed for systems that exhibit rigid coordination to Cu^{2+},[61,80–83] which will lead to lower distribution widths for angles χ, γ and η. Finally, the bandwidth of the pump pulse should be *ca.* 100 MHz or larger. A value of 100 MHz is conservative and can be readily achieved by pump pulses lengths of around 10 ns or using arbitrary waveform generators and resonators on commercial instrumentation. Furthermore, increasing the pump excitation bandwidth to 300 MHz can potentially reduce the DEER acquisition scheme to only 2 fields (*cf.* Fig. S11, ESI†). The acquisition scheme can be reduced further to one field with the recent development of pent loop-gap resonators[84] and ultra-wideband arbitrary waveform generators (*cf.* Fig. S12, ESI†).[85,86]

DEER on liganded hGSTA1-1

We next verified the acquisition scheme experimentally, by collecting DEER data on K211H/E215H hGSTA1-1 mutant which was labelled with Cu^{2+}–NTA. Due to the homodimeric nature of hGSTA1-1, a single dHis mutant provides two labelled sites, one on each subunit, for distance measurements. Fig. 9A shows the FS-ESE spectrum of K211H/E215H hGSTA1-1 and the three pump fields at which DEER was acquired is indicated by solid vertical lines. The values of specific fields are in the Experimental section. We were able to obtain a dipolar evolution time of *ca.* 7 μs due to the long phase memory relaxation time achieved (over 9 μs, *cf.* Fig. S13, ESI†) by deuteration of the solvent and the glycerol as has been recently reported.[87] Such a dipolar evolution time is important to resolve a *ca.* 5.0 nm distance, and is a dramatic improvement over previous efforts where short phase memory times limited the dipolar evolution time to *ca.* 4 μs.[38,87] The primary DEER traces are shown in ESI† (Fig. S14).

The background subtracted DEER data using DEER-Analysis[67] at these fields are shown in Fig. 9B. The time traces are not identical at the three fields, which is a clear indicator of orientational selectivity.

Each time-domain DEER signal was normalized to the intensity of the FS-ESE spectrum (*cf.* Fig. S14, ESI†) and summed to obtain the field average DEER signal (*cf.* inset of Fig. 9C). The background subtracted DEER signal and the fit from Tikhonov regularization is shown in Fig. 9C. Fig. 9D shows the resulting distance distribution using ComparativeDEERAnalyzer (CDA).[88,89] CDA generates a consensus distance distribution and uncertainty estimate using DEERNet and DEERLab analysis programs. DEERNet utilizes a deep neural network and automatically analyzes the contribution to the baseline from intermolecular dipolar interactions, which reduces potential user bias from the analysis.[88] DEERLab is a single step automated

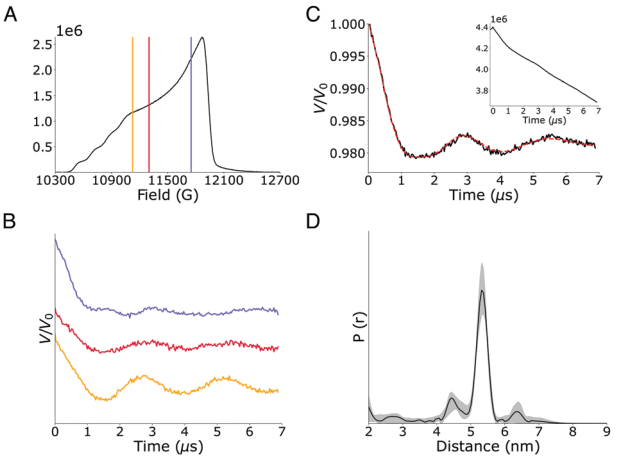

Fig. 9 (A) Field-swept-electron spin echo spectrum of dHis–Cu^{2+}–NTA labeled hGSTA1-1. The magnetic fields for the pump pulses are labeled with color coded vertical lines. (B) The background subtracted DEER time domain at each magnetic field. The data was offset on the *y*-axis for better visualization. (C) The background subtracted average DEER time trace is plotted in black solid line, with Tikhonov fit shown as a red dashed line. The inset is the summed primary DEER time trace. (D) Distance distribution is analyzed by comparative DEER analysis (CDA). The uncertainty in the distribution is shown by grey shading.

fitting program that utilizes Tikhonov regularization, removing all user bias.[89] The uncertainty of the distributions is plotted in grey shading. The individual results from the different analysis programs are provided in ESI† (Fig. S15). A single distance centered around 5.3 nm, labeled by the red dashed vertical line in Fig. S15 (ESI†), was consistently shown by each analysis tool.

To further confirm that three fields are sufficient, we collected 7 more traces at different magnetic fields (*cf.* details in the Experimental section) marked by a blue and six grey vertical lines in Fig. 10A. Fig. 10B shows that collecting one or even seven additional DEER measurements does not change the time trace. The resulting distance distributions, shown in Fig. 10C, are identical within error. This experimental observation is consistent with our DEER simulations where additional DEER does not significantly improve the sampling of θ and the DEER signal (*cf.* Fig. S5, ESI†).

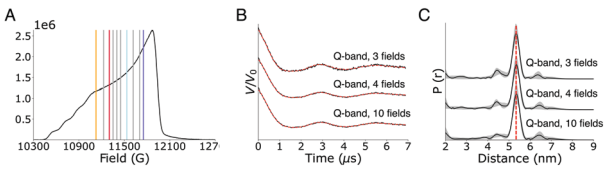

Fig. 10 Comparison of Q-band DEER collected at 3, 4 and 10 magnetic fields. (A) FS-ESE spectrum with DEER time traces collected at one additional magnetic field labeled with blue, and at six more magnetic fields with grey vertical lines. The fields are in addition to the 3 optimal fields that are shown by colored lines in purple, red and yellow. (B) DEER time trace averaged over 3, 4 and 10 magnetic field. The time traces are offset at y-axis for visualization. (C) Distance distribution by CDA. The uncertainty is indicated by the grey shading. The vertical line marks the most probable distance at 5.3 nm. The distance distributions for 3 fields, 4 fields, and 10 fields agree within the uncertainty.

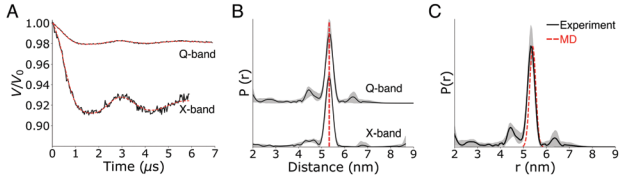

Fig. 11 (A) Summed Q-band DEER signals compared to X-band DEER. The modulation depth for X-band DEER is 7.7%, whereas the Q-band DEER shows a modulation depth of 2.0%. (B) Distance distribution by Consensus DEER analysis of the summed Q-band data compared to the X-band data. The uncertainty is indicated by the grey shading. The most probable distance, shown by the red-dashed line, was the same for X-band and Q-band data. (C) Cu^{2+}–Cu^{2+} distance distribution from MD simulation is compared to the EPR distance distribution. The most probable Cu^{2+}-Cu^{2+} distance by DEER measurement and MD simulation which agree within the uncertainty level of the experiment.

The proposed acquisition scheme is a dramatic improvement of the DEER protocol on commercial instrumentation. Using the optimal scheme, we were able to obtain the expected distance with only three measurements at different magnetic fields. The data collection time at each magnetic fields was between 1 h to 3.5 h, so the total DEER data collection time was *ca.* 7 h. In contrast, seventeen magnetic fields were used to measure the distance on a dHis–Cu^{2+} labeled protein at Q-band.[37] The optimal scheme therefore reduces the cryogens cost and data collection time by at least 5 to 6 fold. Note, however, that the acquisition of data at different fields is useful if orientational information is needed.[37]

X-band DEER and MD results further proves the validity of the summed Q-band DEER

Next, we acquired DEER data at X-band to further validate the Q-band DEER results. For dHis–Cu^{2+} labeling orientational selectivity is minimal at X-band and acquisition at only one field is needed.[31–33,37,55] The DEER time trace at both X-band and Q-band are shown in Fig. 11A. The X-band time trace was collected for *ca.* 6 μs to ensure sufficient signal-to-noise ratio while obtaining enough acquisition time for two modulations of a *ca.* 6.0 nm distance. The X-band time trace shows similar modulation frequency seen in the averaged Q-band signal, and the resulting distance distributions from X-band and Q-band are similar, as shown in Fig. 11B.

Finally, in Fig. 11C we compare the experimental distance distribution with the distribution obtained from MD simulations. The agreement between the two distributions is remarkable. More importantly, this result adds to previous evidence[55] that MD simulations can accurately predict the EPR distance measurements for Cu^{2+}–NTA labeled proteins. The accurate prediction of distances by modeling remains a critical bottleneck for nitroxide labels.[90,91] This body of work therefore foreshadows future work that combine MD simulations with EPR distance constraints to incisively probe protein structure and function.

Conclusions

In this work, we have demonstrated an efficient procedure to perform dHis–Cu^{2+}-based Q-band DEER distance measurements. The optimal acquisition scheme can generate a high-resolution distance distribution with five to six times less collection time. Using a novel Monte-Carlo approach, we established that collecting data with the pump pulses at three magnetic fields (*ca.* 100 G, 580 G and 827 G lower than the maximum of the FS-ESE spectrum) is generally optimal. The summed data from these fields leads to orientational-independent DEER measurements. An additional DEER measurement (at a magnetic field of *ca.* 338 G lower than the maximum of the FS-ESE spectrum) is suggested to allow confident interpretation of the minor features in the distance distributions. Using these three magnetic fields, we collected a high-quality distance distribution for hGSTA1-1 and verified the obtained distribution with data at X-band and MD simulation. Importantly, we demonstrated that performing Q-band DEER measurement at seven additional fields did not show further orientational averaging. This protocol will benefit greatly from recently developed ultra-wideband arbitrary waveform generators[85] and pent loop-gap resonators.[84]

While this work focuses on the DEER using Cu^{2+}-based labels, future application of our Monte-Carlo approach can be applied to ESEEM experiments for Cu^{2+}-based systems that also shows orientational selectivity effects.[92,93] We can also apply this approach to Cu^{2+} distance measurements by alternative pulsed-dipolar spectroscopy techniques.[94,95] Additionally, this approach can be adapted for other Cu^{2+} systems with higher binding affinity[61,80–83] and other paramagnetic spins with large spectral bandwidth such as Co^{2+} and Fe^{3+}.[96,97] Further understanding of the orientational selectivity effect will expand the power of pulsed-EPR techniques and make EPR measurements more resource-conscious and widely accessible to the scientific community.

Author contributions

X. B. performed the experiments, molecular dynamics simulations, and analysed the data. Z. H. wrote the Python program for carrying out the Monte-Carlo simulations and Z. H. and H. R. H. analysed the theoretical results. S. S. conceived the project and supervised all aspects of the work. X. B., Z. H., H. R. H., and S. S. prepared the manuscript. All authors reviewed the manuscript and agreed to the final version of the manuscript.

Conflicts of interest

There are no conflicts to declare.

Acknowledgements

This research was supported by the National Science Foundation [NSF BSF MCB-2006154]. X. B. would like to thank the University of Pittsburgh for the Andrew Mellon Predoctoral Fellowship. The molecular dynamics simulation was carried out at the University of Pittsburgh's Center for Research Computing.

Notes and references

1 M. Pannier, S. Veit, A. Godt, G. Jeschke and H. W. Spiess, Dead-time free measurement of dipole–dipole interactions between electron spins, *J. Magn. Reson.*, 2011, **213**, 316–325.

2 G. Jeschke, M. Pannier, A. Godt and H. W. Spiess, Dipolar spectroscopy and spin alignment in electron paramagnetic resonance, *Chem. Phys. Lett.*, 2000, **331**, 243–252.

3 S. Milikisyants, F. Scarpelli, M. G. Finiguerra, M. Ubbink and M. Huber, A pulsed EPR method to determine distances between paramagnetic centers with strong spectral anisotropy and radicals: The dead-time free RIDME sequence, *J. Magn. Reson.*, 2009, **201**, 48–56.

4 L. V. Kulik, S. A. Dzuba, I. A. Grigoryev and Yu.-D. Tsvetkov, Electron dipole–dipole interaction in ESEEM of nitroxide biradicals, *Chem. Phys. Lett.*, 2001, **343**, 315–324.

5 A. D. Milov, A. G. Maryasov and Y. D. Tsvetkov, Pulsed electron double resonance (PELDOR) and its applications in free-radicals research, *Appl. Magn. Reson.*, 1998, **15**, 107–143.

6 P. P. Borbat and J. H. Freed, Multiple-quantum ESR and distance measurements, *Chem. Phys. Lett.*, 1999, **313**, 145–154.

7 M. Bonora, J. Becker and S. Saxena, Suppression of electron spin-echo envelope modulation peaks in double quantum coherence electron spin resonance, *J. Magn. Reson.*, 2004, **170**, 278–283.

8 O. Dalmas, P. Sompornpisut, F. Bezanilla and E. Perozo, Molecular mechanism of Mg_2^+-dependent gating in CorA, *Nat. Commun.*, 2014, **5**, 3590.

9 A. Collauto, S. Bülow, D. B. Gophane, S. Saha, L. S. Stelzl, G. Hummer, S. T. Sigurdsson and T. F. Prisner, Compaction of RNA Duplexes in the Cell**, *Angew. Chem., Int. Ed.*, 2020, **59**, 23025–23029.

10 R. Dastvan, S. Mishra, Y. B. Peskova, R. K. Nakamoto and H. S. Mchaourab, Mechanism of allosteric modulation of P-glycoprotein by transport substrates and inhibitors, *Science*, 2019, **364**, 689–692.

11 J. L. Kear, M. E. Blackburn, A. M. Veloro, B. M. Dunn and G. E. Fanucci, Subtype Polymorphisms Among HIV-1 Protease Variants Confer Altered Flap Conformations and Flexibility, *J. Am. Chem. Soc.*, 2009, **131**, 14650–14651.

12 C. Altenbach, A. K. Kusnetzow, O. P. Ernst, K. P. Hofmann and W. L. Hubbell, High-resolution distance mapping in rhodopsin reveals the pattern of helix movement due to activation, *Proc. Natl. Acad. Sci. U. S. A.*, 2008, **105**, 7439–7444.

13 T. Hett, T. Zbik, S. Mukherjee, H. Matsuoka, W. Bönigk, D. Klose, C. Rouillon, N. Brenner, S. Peuker, R. Klement, H.-J. Steinhoff, H. Grubmüller, R. Seifert, O. Schiemann and U. B. Kaupp, Spatiotemporal Resolution of Conformational Changes in Biomolecules by Combining Pulsed Electron–Electron Double Resonance Spectroscopy with Microsecond Freeze-Hyperquenching, *J. Am. Chem. Soc.*, 2021, **143**, 6981–6989.

14 E. G.-B. Evans, J. L.-W. Morgan, F. DiMaio, W. N. Zagotta and S. Stoll, Allosteric conformational change of a cyclic nucleotide-gated ion channel revealed by DEER spectroscopy, *Proc. Natl. Acad. Sci. U. S. A.*, 2020, **117**, 10839–10847.

15 E. G.-B. Evans, M. J. Pushie, K. A. Markham, H.-W. Lee and G. L. Millhauser, Interaction between Prion Protein's Copper-Bound Octarepeat Domain and a Charged C-Terminal Pocket Suggests a Mechanism for N-Terminal Regulation, *Structure*, 2016, **24**, 1057–1067.

16 S.-Y. Park, P. P. Borbat, G. Gonzalez-Bonet, J. Bhatnagar, A. M. Pollard, J. H. Freed, A. M. Bilwes and B. R. Crane, Reconstruction of the chemotaxis receptor–kinase assembly, *Nat. Struct. Mol. Biol.*, 2006, **13**, 400–407.

17 T. Schmidt, C. D. Schwieters and G. M. Clore, Spatial domain organization in the HIV-1 reverse transcriptase p66 homodimer precursor probed by double electron-electron resonance EPR, *Proc. Natl. Acad. Sci. U. S. A.*, 2019, **116**, 17809–17816.

18 D. A. Nyenhuis, T. D. Nilaweera, J. K. Niblo, N. Q. Nguyen, K. H. DuBay and D. S. Cafiso, Evidence for the Supramolecular Organization of a Bacterial Outer-Membrane Protein from In Vivo Pulse Electron Paramagnetic Resonance Spectroscopy, *J. Am. Chem. Soc.*, 2020, **142**, 10715–10722.

19 O. A. Krumkacheva, G. Y. Shevelev, A. A. Lomzov, N. S. Dyrkheeva, A. A. Kuzhelev, V. V. Koval, V. M. Tormyshev, Y. F. Polienko, M. V. Fedin, D. V. Pyshnyi, O. I. Lavrik and E. G. Bagryanskaya, DNA complexes with human apurinic/apyrimidinic endonuclease 1: structural insights revealed by pulsed dipolar EPR with orthogonal spin labeling, *Nucleic Acids Res.*, 2019, **47**, 7767–7780.

20 K. M. Stone, J. E. Townsend, J. Sarver, P. J. Sapienza, S. Saxena and L. Jen-Jacobson, Electron Spin Resonance Shows Common Structural Features for Different Classes of *Eco* RI-DNA Complexes, *Angew. Chem.*, 2008, **120**, 10346–10348.

21 D. M. Yin, J. S. Hannam, A. Schmitz, O. Schiemann, G. Hagelueken and M. Famulok, Studying the Conformation of a Receptor Tyrosine Kinase in Solution by Inhibitor-Based Spin Labeling, *Angew. Chem., Int. Ed.*, 2017, **56**, 8417–8421.

22 A. Gamble Jarvi, T. F. Cunningham and S. Saxena, Efficient localization of a native metal ion within a protein by Cu^{2+}-based EPR distance measurements, *Phys. Chem. Chem. Phys.*, 2019, **21**, 10238–10243.

23 D. Abdullin, N. Florin, G. Hagelueken and O. Schiemann, EPR-Based Approach for the Localization of Paramagnetic Metal Ions in Biomolecules, *Angew. Chem.*, 2015, **127**, 1847–1851.

24 P. Roser, M. J. Schmidt, M. Drescher and D. Summerer, Site-directed spin labeling of proteins for distance measurements in vitro and in cells, *Org. Biomol. Chem.*, 2016, **14**, 5468–5476.

25 R. Igarashi, T. Sakai, H. Hara, T. Tenno, T. Tanaka, H. Tochio and M. Shirakawa, Distance Determination in Proteins inside *Xenopus laevis* Oocytes by Double Electron−Electron Resonance Experiments, *J. Am. Chem. Soc.*, 2010, **132**, 8228–8229.

26 M. Teucher, H. Zhang, V. Bader, K. F. Winklhofer, A. J. García-Sáez, A. Rajca, S. Bleicken and E. Bordignon, A new perspective on membrane-embedded Bax oligomers

using DEER and bioresistant orthogonal spin labels, *Sci. Rep.*, 2019, **9**, 13013.

27 A. Martorana, G. Bellapadrona, A. Feintuch, E. Di Gregorio, S. Aime and D. Goldfarb, Probing Protein Conformation in Cells by EPR Distance Measurements using Gd $^{3+}$ Spin Labeling, *J. Am. Chem. Soc.*, 2014, **136**, 13458–13465.

28 W. L. Hubbell, C. J. López, C. Altenbach and Z. Yang, Technological advances in site-directed spin labeling of proteins, *Curr. Opin. Struct. Biol.*, 2013, **23**, 725–733.

29 A. Gamble Jarvi, X. Bogetti, K. Singewald, S. Ghosh and S. Saxena, Going the dHis-tance: Site-Directed Cu $^{2+}$ Labeling of Proteins and Nucleic Acids, *Acc. Chem. Res.*, 2021, **54**, 1481–1491.

30 A. Giannoulis, Y. Ben-Ishay and D. Goldfarb, *Methods in Enzymology*, Elsevier, 2021, vol. 651, pp. 235–290.

31 T. F. Cunningham, M. R. Putterman, A. Desai, W. S. Horne and S. Saxena, The Double-Histidine Cu $^{2+}$ -Binding Motif: A Highly Rigid, Site-Specific Spin Probe for Electron Spin Resonance Distance Measurements, *Angew. Chem.*, 2015, **127**, 6428–6432.

32 M. J. Lawless, S. Ghosh, T. F. Cunningham, A. Shimshi and S. Saxena, On the use of the Cu^{2+}-iminodiacetic acid complex for double histidine based distance measurements by pulsed ESR, *Phys. Chem. Chem. Phys.*, 2017, **19**, 20959–20967.

33 S. Ghosh, M. J. Lawless, G. S. Rule and S. Saxena, The Cu^{2+}-nitrilotriacetic acid complex improves loading of α-helical double histidine site for precise distance measurements by pulsed ESR, *J. Magn. Reson.*, 2018, **286**, 163–171.

34 A. Gamble Jarvi, J. Casto and S. Saxena, Buffer effects on site directed Cu2 + -labeling using the double histidine motif, *J. Magn. Reson.*, 2020, **320**, 106848.

35 J. L. Wort, S. Arya, K. Ackermann, A. J. Stewart and B. E. Bode, Pulse Dipolar EPR Reveals Double-Histidine Motif Cu ^{II} –NTA Spin-Labeling Robustness against Competitor Ions, *J. Phys. Chem. Lett.*, 2021, **12**, 2815–2819.

36 K. Ackermann, J. L. Wort and B. E. Bode, Nanomolar Pulse Dipolar EPR Spectroscopy in Proteins: Cu^{II}–Cu^{II} and Nitroxide–Nitroxide Cases, *J. Phys. Chem. B*, 2021, **125**, 5358–5364.

37 A. Gamble Jarvi, K. Ranguelova, S. Ghosh, R. T. Weber and S. Saxena, On the Use of Q-Band Double Electron–Electron Resonance To Resolve the Relative Orientations of Two Double Histidine-Bound Cu^{2+} Ions in a Protein, *J. Phys. Chem. B*, 2018, **122**, 10669–10677.

38 M. J. Lawless, J. R. Pettersson, G. S. Rule, F. Lanni and S. Saxena, ESR Resolves the C Terminus Structure of the Ligand-free Human Glutathione S-Transferase A1-1, *Biophys. J.*, 2018, **114**, 592–601.

39 H. Sameach, S. Ghosh, L. Gevorkyan-Airapetov, S. Saxena and S. Ruthstein, EPR Spectroscopy Detects Various Active State Conformations of the Transcriptional Regulator CueR, *Angew. Chem.*, 2019, **131**, 3085–3088.

40 K. Singewald, X. Bogetti, K. Sinha, G. S. Rule and S. Saxena, Double Histidine Based EPR Measurements at Physiological Temperatures Permit Site-Specific Elucidation of Hidden Dynamics in Enzymes, *Angew. Chem., Int. Ed.*, 2020, **59**, 23040–23044.

41 M. J. Lawless, J. L. Sarver and S. Saxena, Nucleotide-Independent Copper(II)-Based Distance Measurements in DNA by Pulsed ESR Spectroscopy, *Angew. Chem., Int. Ed.*, 2017, **56**, 2115–2117.

42 S. Ghosh, M. J. Lawless, H. J. Brubaker, K. Singewald, M. R. Kurpiewski, L. Jen-Jacobson and S. Saxena, Cu^{2+}-based distance measurements by pulsed EPR provide distance constraints for DNA backbone conformations in solution, *Nucleic Acids Res.*, 2020, **48**, e49–e49.

43 J. Casto, A. Mandato, L. Hofmann, I. Yakobov, S. Ghosh, S. Ruthstein and S. Saxena, Cu(II)-based DNA labeling identifies the structural link between transcriptional activation and termination in a metalloregulator, *Chem. Sci.*, 2022, **13**, 1693–1697.

44 D. M. Engelhard, A. Meyer, A. Berndhäuser, O. Schiemann and G. H. Clever, Di-copper(II) DNA G-quadruplexes as EPR distance rulers, *Chem. Commun.*, 2018, **54**, 7455–7458.

45 L. M. Stratmann, Y. Kutin, M. Kasanmascheff and G. H. Clever, Precise Distance Measurements in DNA G-Quadruplex Dimers and Sandwich Complexes by Pulsed Dipolar EPR Spectroscopy, *Angew. Chem., Int. Ed.*, 2021, **60**, 4939–4947.

46 M. P. Donohue and V. A. Szalai, Distance measurements between paramagnetic ligands bound to parallel stranded guanine quadruplexes, *Phys. Chem. Chem. Phys.*, 2016, **18**, 15447–15455.

47 H. Ghimire, R. M. McCarrick, D. E. Budil and G. A. Lorigan, Significantly Improved Sensitivity of Q-Band PELDOR/DEER Experiments Relative to X-Band Is Observed in Measuring the Intercoil Distance of a Leucine Zipper Motif Peptide (GCN4-LZ), *Biochemistry*, 2009, **48**, 5782–5784.

48 A. Schweiger and G. Jeschke, *Principles of pulse electron paramagnetic resonance*, Oxford University Press on Demand, 2001.

49 K. Singewald, J. A. Wilkinson and S. Saxena, Copper Based Site-directed Spin Labeling of Proteins for Use in Pulsed and Continuous Wave EPR Spectroscopy, *Bio-Protoc.*, 2021, **11**, e4258–e4258.

50 D. C. Kuhnert, Y. Sayed, S. Mosebi, M. Sayed, T. Sewell and H. W. Dirr, Tertiary Interactions Stabilise the C-terminal Region of Human Glutathione Transferase A1-1: a Crystallographic and Calorimetric Study, *J. Mol. Biol.*, 2005, **349**, 825–838.

51 I. Le Trong, R. E. Stenkamp, C. Ibarra, W. M. Atkins and E. T. Adman, 1.3-Å resolution structure of human glutathione S-transferase with S-hexyl glutathione bound reveals possible extended ligandin binding site: hGSTA1-1 With GTX, *Proteins: Struct., Funct., Bioinf.*, 2002, **48**, 618–627.

52 C. I. Bayly, P. Cieplak, W. Cornell and P. A. Kollman, A well-behaved electrostatic potential based method using charge restraints for deriving atomic charges: the RESP model, *J. Phys. Chem.*, 1993, **97**, 10269–10280.

53 A. Jakalian, B. L. Bush, D. B. Jack and C. I. Bayly, Fast, efficient generation of high-quality atomic charges. AM1-BCC model: I. Method, *J. Comput. Chem.*, 2000, **21**, 132–146.

54 J. Wang, R. M. Wolf, J. W. Caldwell, P. A. Kollman and D. A. Case, Development and testing of a general amber force field, *J. Comput. Chem.*, 2004, **25**, 1157–1174.

55 X. Bogetti, S. Ghosh, A. Gamble Jarvi, J. Wang and S. Saxena, Molecular Dynamics Simulations Based on Newly Developed Force Field Parameters for Cu $^{2+}$ Spin Labels Provide Insights into Double-Histidine-Based Double Electron–Electron Resonance, *J. Phys. Chem. B*, 2020, **124**, 2788–2797.
56 D. Case, I. Ben-Shalom, S. Brozell, D. Cerutti, T. Cheatham III, V. Cruzeiro, T. Darden, R. Duke, D. Ghoreishi, M. Gilson and others, *AMBER*, Univ. Calif. San Franc, 2018.
57 W. L. Jorgensen, J. Chandrasekhar, J. D. Madura, R. W. Impey and M. L. Klein, Comparison of simple potential functions for simulating liquid water, *J. Chem. Phys.*, 1983, **79**, 926–935.
58 H. J.-C. Berendsen, J. P.-M. Postma, W. F. van Gunsteren, A. DiNola and J. R. Haak, Molecular dynamics with coupling to an external bath, *J. Chem. Phys.*, 1984, **81**, 3684–3690.
59 R. G. Van and F. Drake, *Python 3 reference manual, Scotts Val. CA Creat.*, 2009, vol. 10, p. 1593511.
60 W. R. Hagen, *Biomolecular EPR Spectroscopy*, CRC Press, 0 edn, 2008.
61 Z. Yang, D. Kise and S. Saxena, An Approach towards the Measurement of Nanometer Range Distances Based on Cu^{2+} Ions and ESR, *J. Phys. Chem. B*, 2010, **114**, 6165–6174.
62 A. Maryasov, Y. D. Tsvetkov and J. Raap, Weakly coupled radical pairs in solids: ELDOR in ESE structure studies, *Appl. Magn. Reson.*, 1998, **14**, 101–113.
63 W. B. Mims, Envelope Modulation in Spin-Echo Experiments, *Phys. Rev. B: Solid State*, 1972, **5**, 2409–2419.
64 W. B. Mims, Amplitudes of Superhyperfine Frequencies Displayed in the Electron-Spin-Echo Envelope, *Phys. Rev. B: Solid State*, 1972, **6**, 3543–3545.
65 S. Stoll and A. Schweiger, EasySpin, a comprehensive software package for spectral simulation and analysis in EPR, *J. Magn. Reson.*, 2006, **178**, 42–55.
66 C. E. Tait and S. Stoll, Coherent pump pulses in Double Electron Electron Resonance spectroscopy, *Phys. Chem. Chem. Phys.*, 2016, **18**, 18470–18485.
67 G. Jeschke, V. Chechik, P. Ionita, A. Godt, H. Zimmermann, J. Banham, C. R. Timmel, D. Hilger and H. Jung, DeerAnalysis2006—a comprehensive software package for analyzing pulsed ELDOR data, *Appl. Magn. Reson.*, 2006, **30**, 473–498.
68 Y. Zhan and G. S. Rule, Glutathione Induces Helical Formation in the Carboxy Terminus of Human Glutathione Transferase A1-1, *Biochemistry*, 2004, **43**, 7244–7254.
69 E. Grahn, M. Novotny, E. Jakobsson, A. Gustafsson, L. Grehn, B. Olin, D. Madsen, M. Wahlberg, B. Mannervik and G. J. Kleywegt, New crystal structures of human glutathione transferase A1-1 shed light on glutathione binding and the conformation of the C-terminal helix, *Acta Crystallogr., Sect. D: Biol. Crystallogr.*, 2006, **62**, 197–207.
70 M. Ji, S. Ruthstein and S. Saxena, Paramagnetic Metal Ions in Pulsed ESR Distance Distribution Measurements, *Acc. Chem. Res.*, 2014, **47**, 688–695.
71 A. Gamble Jarvi, A. Sargun, X. Bogetti, J. Wang, C. Achim and S. Saxena, Development of Cu^{2+}-Based Distance Methods and Force Field Parameters for the Determination of PNA Conformations and Dynamics by EPR and MD Simulations, *J. Phys. Chem. B*, 2020, **124**, 7544–7556.
72 S. Pornsuwan, C. E. Schafmeister and S. Saxena, Analysis of the Dynamical Flexibility of Bis-peptide Nanostructures, *J. Phys. Chem. C*, 2008, **112**, 1377–1384.
73 A. Tannús and M. Garwood, Improved Performance of Frequency-Swept Pulses Using Offset-Independent Adiabaticity, *J. Magn. Reson., Ser. A*, 1996, **120**, 133–137.
74 M. G. Savelieff, T. D. Wilson, Y. Elias, M. J. Nilges, D. K. Garner and Y. Lu, Experimental evidence for a link among cupredoxins: Red, blue, and purple copper transformations in nitrous oxide reductase, *Proc. Natl. Acad. Sci. U. S. A.*, 2008, **105**, 7919–7924.
75 R. H. Holm, P. Kennepohl and E. I. Solomon, Structural and Functional Aspects of Metal Sites in Biology, *Chem. Rev.*, 1996, **96**, 2239–2314.
76 J. Peisach and W. E. Blumberg, Structural implications derived from the analysis of electron paramagnetic resonance spectra of natural and artificial copper proteins, *Arch. Biochem. Biophys.*, 1974, **165**, 691–708.
77 J. L. Wort, K. Ackermann, A. Giannoulis, A. J. Stewart, D. G. Norman and B. E. Bode, Sub-Micromolar Pulse Dipolar EPR Spectroscopy Reveals Increasing Cu^{II} -labelling of Double-Histidine Motifs with Lower Temperature, *Angew. Chem.*, 2019, **131**, 11807–11811.
78 J. L. Wort, K. Ackermann, D. G. Norman and B. E. Bode, A general model to optimise Cu^{II} labelling efficiency of double-histidine motifs for pulse dipolar EPR applications, *Phys. Chem. Chem. Phys.*, 2021, **23**, 3810–3819.
79 S. Ghosh, J. Casto, X. Bogetti, C. Arora, J. Wang and S. Saxena, Orientation and dynamics of Cu^{2+} based DNA labels from force field parameterized MD elucidates the relationship between EPR distance constraints and DNA backbone distances, *Phys. Chem. Chem. Phys.*, 2020, **22**, 26707–26719.
80 A. M. Bowen, M. W. Jones, J. E. Lovett, T. G. Gaule, M. J. McPherson, J. R. Dilworth, C. R. Timmel and J. R. Harmer, Exploiting orientation-selective DEER: determining molecular structure in systems containing Cu(II) centres, *Phys. Chem. Chem. Phys.*, 2016, **18**, 5981–5994.
81 E. Narr, A. Godt and G. Jeschke, Selective Measurements of a Nitroxide–Nitroxide Separation of 5 nm and a Nitroxide–Copper Separation of 2.5 nm in a Terpyridine-Based Copper(II) Complex by Pulse EPR Spectroscopy, *Angew. Chem., Int. Ed.*, 2002, **41**, 3907–3910.
82 B. E. Bode, J. Plackmeyer, T. F. Prisner and O. Schiemann, PELDOR Measurements on a Nitroxide-Labeled Cu(II) Porphyrin: Orientation Selection, Spin-Density Distribution, and Conformational Flexibility, *J. Phys. Chem. A*, 2008, **112**, 5064–5073.
83 J. E. Lovett, A. M. Bowen, C. R. Timmel, M. W. Jones, J. R. Dilworth, D. Caprotti, S. G. Bell, L. L. Wong and J. Harmer, Structural information from orientationally selective DEER spectroscopy, *Phys. Chem. Chem. Phys.*, 2009, **11**, 6840.
84 R. Tschaggelar, F. D. Breitgoff, O. Oberhänsli, M. Qi, A. Godt and G. Jeschke, High-Bandwidth Q-Band EPR Resonators, *Appl. Magn. Reson.*, 2017, **48**, 1273–1300.

85 A. Doll and G. Jeschke, Fourier-transform electron spin resonance with bandwidth-compensated chirp pulses, *J. Magn. Reson.*, 2014, **246**, 18–26.
86 F. D. Breitgoff, K. Keller, M. Qi, D. Klose, M. Yulikov, A. Godt and G. Jeschke, UWB DEER and RIDME distance measurements in Cu(II)–Cu(II) spin pairs, *J. Magn. Reson.*, 2019, **308**, 106560.
87 J. Casto, A. Mandato and S. Saxena, dHis-troying Barriers: Deuteration Provides a Pathway to Increase Sensitivity and Accessible Distances for Cu^{2+} Labels, *J. Phys. Chem. Lett.*, 2021, **12**, 4681–4685.
88 S. G. Worswick, J. A. Spencer, G. Jeschke and I. Kuprov, Deep neural network processing of DEER data, *Sci. Adv.*, 2018, **4**, eaat5218.
89 L. Fábregas Ibáñez, G. Jeschke and S. Stoll, DeerLab: a comprehensive software package for analyzing dipolar electron paramagnetic resonance spectroscopy data, *Magn. Reson.*, 2020, **1**, 209–224.
90 J. L. Sarver, J. E. Townsend, G. Rajapakse, L. Jen-Jacobson and S. Saxena, Simulating the Dynamics and Orientations of Spin-Labeled Side Chains in a Protein–DNA Complex, *J. Phys. Chem. B*, 2012, **116**, 4024–4033.
91 M. I. Fajer, H. Li, W. Yang and P. G. Fajer, Mapping Electron Paramagnetic Resonance Spin Label Conformations by the Simulated Scaling Method, *J. Am. Chem. Soc.*, 2007, **129**, 13840–13846.
92 H. L. Flanagan, G. J. Gerfen, A. Lai and D. J. Singel, Orientation-selective ^{14}N electron spin echo envelope modulation (ESEEM): The determination of ^{14}N quadrupole coupling tensor principal axis orientations in orientationally disordered solids, *J. Chem. Phys.*, 1988, **88**, 2162–2168.
93 W. A. Gunderson, J. Hernández-Guzmán, J. W. Karr, L. Sun, V. A. Szalai and K. Warncke, Local Structure and Global Patterning of Cu^{2+} Binding in Fibrillar Amyloid-β [Aβ(1–40)] Protein, *J. Am. Chem. Soc.*, 2012, **134**, 18330–18337.
94 A. Meyer, D. Abdullin, G. Schnakenburg and O. Schiemann, Single and double nitroxide labeled bis(terpyridine)-copper(II): influence of orientation selectivity and multispin effects on PELDOR and RIDME, *Phys. Chem. Chem. Phys.*, 2016, **18**, 9262–9271.
95 S. Ruthstein, M. Ji, P. Mehta, L. Jen-Jacobson and S. Saxena, Sensitive Cu^{2+}–Cu^{2+} Distance Measurements in a Protein–DNA Complex by Double-Quantum Coherence ESR, *J. Phys. Chem. B*, 2013, **117**, 6227–6230.
96 C. Elsässer, M. Brecht and R. Bittl, Pulsed Electron−Electron Double Resonance on Multinuclear Metal Clusters: Assignment of Spin Projection Factors Based on the Dipolar Interaction, *J. Am. Chem. Soc.*, 2002, **124**, 12606–12611.
97 A. Giannoulis, C. L. Motion, M. Oranges, M. Bühl, G. M. Smith and B. E. Bode, Orientation selection in high-field RIDME and PELDOR experiments involving low-spin Co^{II} ions, *Phys. Chem. Chem. Phys.*, 2018, **20**, 2151–2154.